Copernicus (CMEMS) operational model intercomparison in the western Mediterranean Sea: Insights from an eddy tracker

Evan Mason[1,2], Simón Ruiz[1], Romain Bourdalle-Badie[3], Guillaume Reffray[3], Marcos García-Sotillo[4], and Ananda Pascual[1]

[1]IMEDEA, Esporles, Mallorca, Spain
[2]University of Washington, Seattle, USA
[3]Mercator Ocean, 8-10 Rue Hermès, 31520, Ramonville Saint-Agne, France
[4]Puertos del Estado, Madrid, Spain

Correspondence to: Evan Mason (emason@imedea.uib-csic.es)

Abstract. Rapid evolution of operational ocean models is driven by advances in numerics and sophisticated data assimilation schemes, computational power, and storage capacity. The Copernicus Marine Service (CMEMS) is a major provider of operational products that are made available through an online catalogue. The service includes global and regional forecasts in near-real-time and reanalysis modes. Here we apply an

5 eddy tracker to daily SSH fields from three such reanalysis products from the CMEMS catalogue, with the objective to evaluate their performance in terms of their eddy properties and three-dimensional composite structures over the period 2013 through 2016. The products are (i) the Global Analysis Forecast, (ii) the Mediterranean Analysis Forecast, and (iii) the Iberia-Biscay-Ireland Analysis Forecast. The common domain between these reanalyses is the western Mediterranean Sea (WMED) between the Strait of Gibraltar

10 and Sardinia. This is a complex region with strong density gradients, especially in the Alboran Sea in the west where Atlantic and Mediterranean waters compete. Surface eddy property maps over the WMED of eddy radii, amplitudes and nonlinearity are consistent between the models, as well as with gridded altimetric data that serve as a reference. Mean 3D eddy composites are shown only for three subregions in the Alboran Sea. These are mostly consistent between the models, with minor differences being attributed to details of

15 the respective model configurations. This information can be informative for the ongoing development of these CMEMS operational modeling systems.

Copyright statement. TEXT

1 Introduction

The Copernicus Marine Environment Monitoring Service (CMEMS) is a reference portal that supplies information about the physical state and variability of the global ocean and regional seas (Von Schukmann et al., 2016; Le Traon et al., 2017). CMEMS distributes remote sensing and $in\ situ$ observations, and short-term model forecasts in response to the needs of European public and private users. Specific products are delivered within four distinct areas (e.g., diagnostic analyses, forecasts, etc): marine resources; marine safety; coastal and marine environment and weather; and seasonal forecasts and climate.

The CMEMS architecture includes seven Monitoring and Forecasting Centers (MFC) that generate operational products such as short-term forecasts, hindcasts and reanalyses in different areas of the European seas (Arctic Ocean, Baltic Sea, northwest European shelves, Iberia-Biscay-Ireland area, and the Mediterranean and Black Seas). Additionally, there is a global MFC that delivers products at global ocean scale. A detailed description of each of the seven MFCs can be found in Le Traon et al. (2017). The quality of the products from these operational systems is crucial because they are used, together with observations, to detect and analyse environmental and climate change. In that sense, a continuous effort to improve CMEMS products is made through new research and development projects funded by the CMEMS service evolution STA (2017).

There are three recognised MFCs that produce short-term forecasts for the entire or partial Mediterranean Sea: (i) the Mediterranean Forecasting System (*MFS*), (ii) the Global Mercator model (*GLO*), and (iii) the Iberia-Biscay-Ireland system (*IBI*); *IBI* covers only the western Mediterranean. As in other regions of the European seas, improvement of the short-term forecasts in the western Mediterranean (WMED) has been a priority for the Service Evolution. To develop the service and produce better forecasts of the ocean in this particular area and in the global ocean in general, we need to increase our understanding of 2D and 3D ocean circulation, dynamics and interactions at different scales, namely the mesoscale (10-100 km) and fine scale (1-10 km). Simulating dynamics at these scales with numerical models is challenging; trade-offs are made between the need for accurate representation of topography and grid resolution (both of which impact volume transport); impact of inclusion of tidal forcing; the need for assimilation, among other factors.

The Mediterranean Sea is often described as an easily-accessible reduced-scale ocean laboratory which hosts almost all of the physical phenomena found in different regions of the global ocean. These processes, which include deep convection (Leaman and Schott, 1991; Herrmann et al., 2009), shelf-slope exchange (Bethoux and Gentili, 1999), thermohaline circulation and water mass interaction (Bergamasco and Malanotte-Rizzoli, 2011, and references therein)), mesoscale (Robinson and Golnaraghi, 1994) and submesoscale dynamics (Bosse et al., 2015), can be sampled and investigated at smaller scales.

In the western Mediterranean (Fig. 1.1), the Alboran Sea is characterized by the presence of two anti-cyclonic gyres (Vargas-Yáñez et al., 2002; Renault et al., 2012) and their associated strong fronts (Tintoré et al., 1988; Allen et al., 2001), that are mostly governed by salinity. In the transition region between the Alboran Sea and the Algerian sub-basin, intense eddies and fronts are also generated although they are less frequent than in the Alboran Sea Pascual et al. (2017). The presence of large eddies in the Algerian basin has been documented by Puillat et al. (2002) and Ruiz et al. (2001). More recently, studies in this basin using high-resolution observations (Cotroneo et al., 2016; Aulicino et al., 2018)) have demonstrated the presence of fine-scale features associated with the large eddies. Regarding the Balearic Sea, the spatial-temporal variability of the surface circulation was investigated by Mason and Pascual (2013) revealing intense mesoscale eddy activity in the sub-basin.

The aim of this paper is to evaluate the performance of three CMEMS operational oceanic models in the western Mediterranean using a subregional three-dimensional (3D) eddy compositing approach. We use an eddy tracker to identify daily positions and sizes (radius, amplitude) of mesoscale eddies in each model solution (Sec. 2). This information allows estimation of indices to extract 3D arrays of data (e.g., temperature, salinity, currents) that extend a horizontal distance of $8\times$ the eddy radius, and from the surface to the ocean floor. Selective averaging of these data *cubes* allows generation of 3D eddy composites covering specified defined subregions such as, for example, the gyres of the Alboran Sea. The paper is structured as follows. The eddy tracking and compositing methodology is described in Sec. 2. Results in Sec. 3 comprise an analysis of eddy properties from the models and altimetry over the western Mediterranean; this followed by a subregional 3D eddy compositing analysis that is focused on the Alboran Sea. (Results from other subregions in the WMED are included in Supp. 2.5). Finally, Sec. 4 is devoted to the discussion and final conclusions of this study.
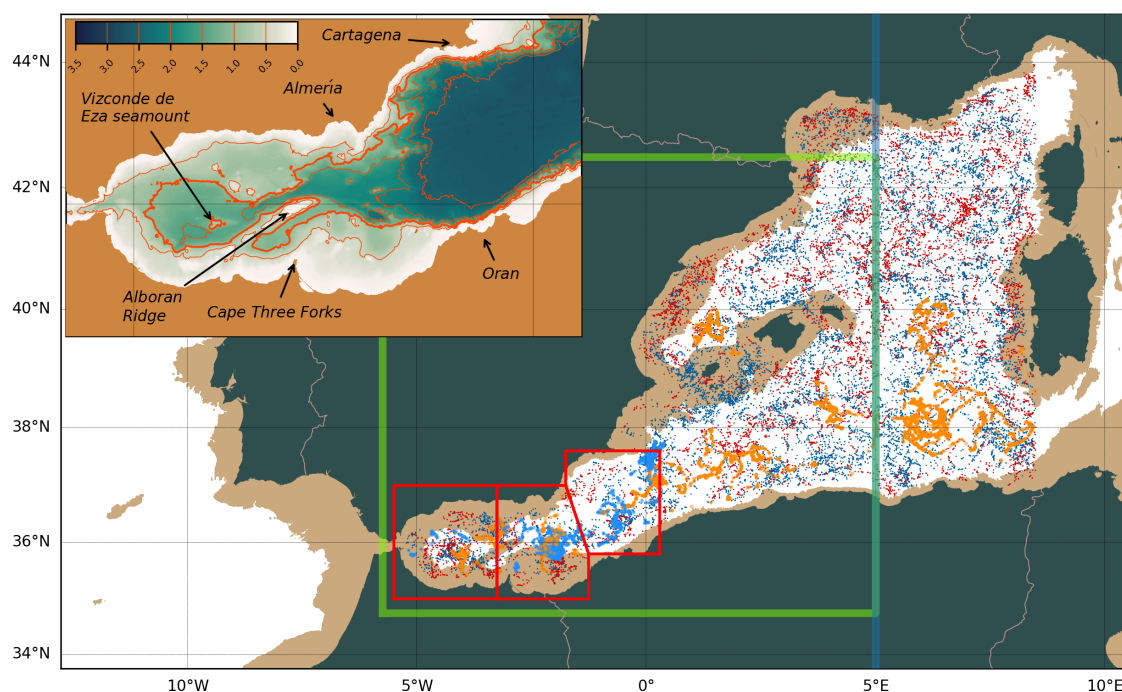
Figure 1. Map of the western Mediterranean study region. Cyclonic and anticyclonic eddy tracks from gridded altimetry are plotted in blue and red, respectively, for the period 2013 to 2016; tracks with lifetimes greater than one year are highlighted in light blue and orange. Brown shading indicates bathymetry shallower than 1000 m. The green box shows the domain used for the eddy property analysis in Sec. 3.1. The blue line marks the eastern boundary of the *IBI* model domain. The areas marked in red in the Alboran Sea indicate the three subregional domains used for eddy compositing in Sec. 3.2. The inset map provides further detail of the topography and relevant physical features of the Alboran Sea.

2 Data and methods

2.1 The CMEMS models

The numerical code used for all three CMEMS models under analysis is the Nucleus for European Modeling of the Ocean (NEMO, e.g., Madec, 2008). NEMO solves the three-dimensional finite-difference primitive equations in spherical coordinates on an Arakawa-C grid and a vertical z-coordinate scheme. It assumes hydrostatic equilibrium and the Boussinesq approximation and makes use of a non-linear split-explicit free surface to simulate fast external gravity waves such as tidal motions. Steep slopes (common in the enclosed western Mediterranean) are well resolved by the use of partial bottom cells to represent the bathymetry (e.g., Barnier et al., 2006).

10   The main characteristics of these products are listed in Tab. 1. Daily mean prognostic variables for the period 1 January 2013 to 30 June 2016 from each product were downloaded by *ftp* from the Copernicus CMEMS portal (http://marine.copernicus.eu/). The data are provided on regular grids. Delivered products are bilinearly interpolated onto a regular longitude/latitude 1/36° grid. The stated general objectives for these forecast model products is to produce near-real-time short-term (5-10 days) forecasts of currents and other oceanographic variables such as temperature, salinity and sea level, that will enable quicker responses to oil spills and other emergencies at sea, as well as support for efforts to achieve better understanding of ocean dynamics.

2.1.1 Mercator Global (*GLO*; GLOBAL_ANALYSIS_FORECAST_PHY_001_024)

The Mercator Global Ocean forecasting system is produced by Mercator Ocean (France) (e.g., Hernandez et al., 2015). The simulation has a horizontal resolution of 1/12° and 50 vertical z-levels. The model includes multivariate data assimilation, which consists of a Singular Extended Evolutive Kalman (SEEK) filter analysis of along-track satellite SLA and sea surface temperature (SST) together with *in situ* profiles of temperature and salinity. The altimeter reference period for the assimilated SLA is 20 years Rio et al. (2014). The assimilated SST is taken from the CMEMS TAC daily level-4 OSTIA composite product Rio et al. (2014). In the Gibraltar Strait there is relaxation of temperature and salinity towards Levitus 2013 values (Locarnini et al., 2013; Zweng et al., 2013). The bathymetry used in the system is a combination of the ETOPO1 (Amante and Eakins, 2009) and GEBCO8 (Becker et al., 2009) topography databases: ETOPO1

Table 1. Main characteristics of the three CMEMS models. Model resolutions are given in degrees; equivalents in km
for the Mediterranean are included in parentheses).

	GLO	*MFS*	*IBI*
Resolution (°)	$1/12$ (~7 km)	$1/16$ (~4 km)	$1/36$ (~2 km)
Vertical levels	50	72	50
Surface forcing	3-hourly; ECMWF	6-hourly; ECMWF	
Boundary forcing	N/A	*GLO*	*GLO*
Rivers	Dai et al. (2009) database	Global Runoff Data Centre (Fekete et al., 1999)	Daily/monthly blend
Version NEMO	3.1	3.6	3.6
Tides	No	No	Yes
Data assimilation	Yes (T/S, SLA, SST)	Yes (T/S, SLA, SST)	No
DA-MDT	Yes	Yes	N/A
Ice	Yes	N/A	N/A
Topography	GEBCO8>200 m, ETOPO1<300 m	GEBCO30	GEBCO, ETOPO, ???

(GEBCO8) is used in regions deeper (shallower) than 300 (200) m with linear interpolation over the 200-300
m layer.

2.1.2 Mediterranean Forecast System (*MFS*; MEDSEA_ANALYSIS_FORECAST_PHYS_006_001)

Produced by the Mediterranean Forecasting System (Italy). Its spatial horizontal resolution is 1/16°, with 72
unevenly spaced vertical z-levels. The MFS product includes data assimilation (based on a 3DVAR scheme)
of temperature and salinity vertical profiles and along-track satellite SLA observations (Dobricic and Pinardi,
2008; Dombrowsky et al., 2009; Tonani et al., 2015). The 20-year mean dynamic topography of Rio et al.
(2014) is used for the assimilation of along-track SLA.

2.1.3 Iberia-Biscay-Ireland (*IBI*; IBI_ANALYSIS_FORECAST_PHYS_005_001)

IBI is developed by Mercator Ocean but is operated by the Spanish Port Authority (Puertos del Estado, Spain) and, although the model domain mainly corresponds to the northeastern Atlantic Ocean, the output simulation also covers the WMED to as far as the 5°E meridian (blue line in Fig. 1.1). The model grid is a
5   subset of the Global 1/12° ORCA tripolar grid also used by the parent system (that provides initial and lateral boundary conditions) but refined to 1/36° horizontal resolution (∼2 km). The system is based on an eddy-resolving NEMO model application run at 1/36° horizontal resolution with 50 vertical z-levels. *IBI* does not include data assimilation; however a downscaling methodology is applied that improves the solution near to the open boundaries and the coasts (Sotillo et al., 2015; Aznar et al., 2016). Lateral open boundary data
10   (temperature, salinity, velocities, and sea level) are interpolated from the daily *GLO* outputs (Sec. 2.1.1). These are complemented by 11 tidal harmonics (M2, S2, N2, K1, O1, Q1, M4, K2, P1, Mf, Mm) built from FES2004 (Lyard et al., 2006) and TPXO7.1 (Egbert and Erofeeva, 2002) tidal model solutions. River runoff consists of a combination of daily observations (PREVIMER project), simulated data (SMHI E-HYPE model), a monthly climatology (GRDC), and the Banque Hydro dataset.

15   ## 2.2   Altimetry

The Mediterranean Sea gridded altimetry product from CMEMS is used to make an observational reference eddy track dataset. The daily sea level anomaly (SLA) along-track satellite observations are interpolated onto a 0.125°×0.125° grid. The spatial correlation lengthscales used for this regional product are set to ∼100 km, which is at the lower end of the range used for its global 0.25° counterpart (∼90-150 km) (Pujol et al., 2016).

20   ## 2.3   Eddy tracking

Version 3.0 of the *py-eddy-tracker*, a sea-surface-height based mesoscale eddy identification and tracking code developed by Mason et al. (2014), was applied to the daily SLA fields from altimetry and the three CMEMS models for the period 01/01/2013 to 30/06/2016. As the models provide the sea surface height (SSH), respective daily model SLA fields were obtained by taking the differences between daily model
25   SSH and SSH means over the study period. The *py-eddy-tracker* uses an SSH-based contouring approach to eddy identification that is similar to the procedures described by Chelton et al. (2011). The eddy tracker

was configured to detect a wide range of eddy sizes and shapes . The same tuning parameters are used for each product, although the different grid resolutions (and relatively coarse correlation length scales used for *ALT*) between the products implies that the scales of detected eddy features will differ. The minimum and maximum parameter values were, for L_e, 0.15°/1.5° and, for A, 0/150 cm. The shape error (Kurian et al., 2011) was 65%. The effective radius (L_e) and amplitude (A) parameters impose minimum and maximum eddy sizes, while the shape error (Kurian et al., 2011) excludes filaments and other elongated closed-contour structures that may not correspond to eddies.

Time dependent outputs from the eddy tracker include eddy position, a speed-based (inner) radius (L) and an effective (outer) radius (L_e), amplitude (A), swirl speed (U) and eddy kinetic energy. Two useful ratios that can be obtained from these eddy properties are nonlinearity (U/c, where c is the eddy propagation speed) and eddy intensity (A/L). Nonlinearity (N) provides a measure of an eddy's capacity to trap fluid within its center; this occurs at values greater than unity (e.g., Chelton et al., 2011). Eddy intensity (EI) is a potential proxy for the presence of elevated vertical motions (e.g., Frenger et al., 2015; Mason et al., 2017).

2.4 Eddy compositing

Eddy compositing of the model prognostic variables was carried out following the procedures described by Mason et al. (2017). For a given variable p (e.g., anomalies of temperature or salinity), we make three-dimensional averages (or eddy composites) for each subregion. The core variables common to each model are potential temperature (T), salinity (S), SSH (η), and u and v velocity components. Model topography was available from *GLO* and *IBI*, and these were also interpolated to the composite grid.

Three additional external variables are included in the compositing:

- The normalized relative vorticity (ζ/f) is derived from u and v, with $\zeta = \frac{\partial v}{\partial x} - \frac{\partial u}{\partial y}$ and f the Coriolis frequency. (The ζ operation is performed on the respective regular model grids, with ∂x and ∂y calculated using the haversine formula.)

- *MFS* includes a mixed layer depth (MLD) variable based on the 0.03 kg m^{-3} density criterion of de Boyer Montégut et al. (2004) and D'Ortenzio et al. (2005). To enable an MLD intercomparison, MLDs from each model are estimated using a different algorithm that is also based on density (Sec. 2.6).
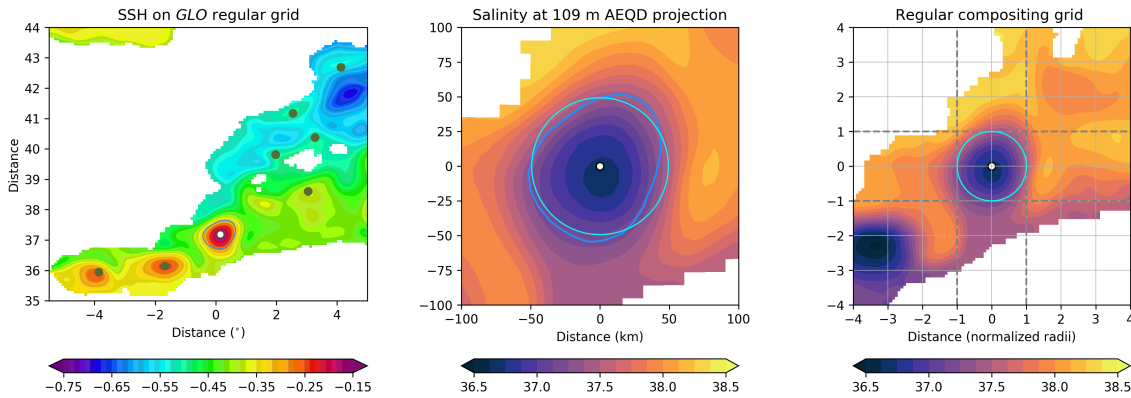
Figure 2. Illustration of the sequential compositing methodology using example SSH and salinity fields from *GLO* on 13/09/2013. (a) SSH is plotted on a regular grid over the western Mediterranean eddy tracking domain. The most intense of several eddy-tracker-identified anticyclones is marked in white near $0°$E, $37°$N and its corresponding speed-based contour is plotted in blue; eddy intensity is determined by the ratio $^A/_L$. Other identified eddies are marked in green. (b) A zoom over the intense eddy of *GLO* salinity at 109 m plotted on an azimuthal equidistant projection (AEQD) shows the fresh salinity anomaly associated with the eddy. Light blue circle corresponds to the radius of the eddy. (c) The salinity field interpolated from the AEQD grid to a regular grid in a normalized eddy radius coordinate. Gray dashed lines highlight the radial extent of the eddy.

– Topography from the $1'$ based Shuttle Radar Topography Mission (SRTM) dataset (Smith and Sandwell, 1997; Becker et al., 2009) is used as an intercomparison reference.

2.5 Eddy vertical tilt correction

We use a simple methodology to estimate eddy tilt. For every eddy observation, starting from the position
5 of the eddy center at the surface level, the indices i, j to the maximum of $|\varsigma/f|$ at each model depth level are estimated. These indices provide (i) a means to estimate the distance at each level between the dynamical center of the eddy and its position as determined by the eddy tracker, and (ii) the possibility to reconstruct each eddy variable (temperature, salinity, etc.) so that each level is aligned horizontally with the position of $|\varsigma/f|$. Illustrative figures of the impact on profile sections of ς, T and S are provided in Supp. **??**; these can
10 be compared with Figs. 3.5, 3.6 and 3.7 in Sec. 3.

2.6 MLD estimation

Mixed layer depth estimates were made by applying the density algorithm developed by Holte and Talley
(2009) to *GLO*, *MFS* and *IBI* temperature and salinity profiles. The *MFS* MLD is also computed online with
the density algorithm of de Boyer Montégut et al. (2004). The estimated MLD data were all passed through
5 the compositing procedure outlined in Sec. 2.4, and their range and variability is shown in Sec. 2.6.

3 Results

3.1 Eddy properties

Eddy property information covers data obtained directly from the eddy tracker, namely eddy position in time
and space, radius, amplitude and swirl speed (e.g., Mason et al., 2014).

10 ### 3.1.1 Eddy tracks

Tracks of detected eddies in the western Mediterranean indicate that the longest-lived eddies are found in the
south in the Alboran Sea and Algerian Basin (Fig. 3.1). Anticyclones tend to be longer-lived than cyclones.
The quantity and duration of long-lived eddies is highest in *ALT* and lowest in *IBI*. There are fewer *ALT*
eddies than in the models. The long-lived *ALT* eddies are concentrated inside the Alboran gyres and the
15 Algerian Basin. There are also a number of long-lived *ALT* anticyclones in the Balearic Sea. *GLO* and *MFS*
have similar patterns of eddy distribution to *ALT*, but they have greater numbers of shorter-lived eddies.
Large numbers of eddies are detected and tracked in *IBI* but they are generally of shorter duration than in
the other products.

3.1.2 Eddy amplitude, radius and intensity

20 High levels of correspondence are found in eddy amplitude and radius distributions from the three models
and altimetry over the western Mediterranean study region (Fig. 3.2). Maps of mean eddy amplitude show
that larger amplitudes are found consistently across the southern regions (up to ~10 cm), and especially in
the gyres of the Alboran Sea where amplitudes are ~10 cm (Fig. 3.2a-h). Anticyclones in the south tend to
have larger amplitudes and are more prevalent than cyclones which, aside from *IBI*, are somewhat smaller
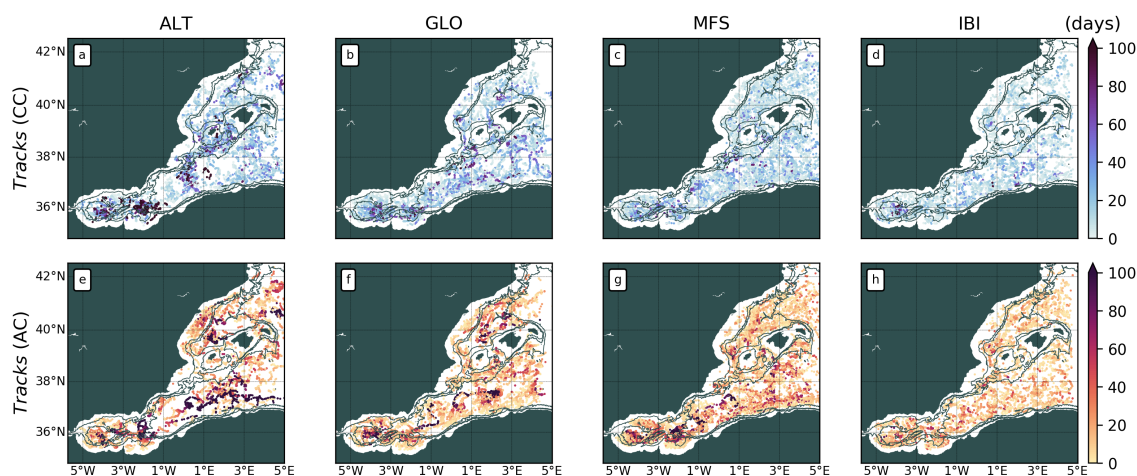
Figure 3. Scatter plots of (top row) cyclonic and (bottom row) anticyclonic eddy observations in the western Mediterranean from altimetry and the three CMEMS models between 2013 and 2016. Colors indicate eddy age between 0 and 100+ days. Topographic contours from SRTM are plotted in gray at 500, 1000, 2000, 4000 m.

outside of the Alboran Sea. The distributions of the amplitude patterns between the products are quite similar for anticyclones, but the cyclones in *IBI* (Fig. 3.2d) have noticeably higher amplitudes along the Algerian current axis than they do in the other products. In the Balearic Sea to the north typical amplitude values are smaller at around 2.5 cm. There are only small differences between cyclones and anticyclones. Extreme
5 amplitudes (>15 cm) are noticeable in the anticyclones of *ALT* and *GLO* at ∼37°N, 0°E (Fig. 3.2e,f). This position corresponds to the Jason-1/Jason-2 satellite track which could explain detection of a strong eddy amplitude signal in this region; *GLO* assimilates altimetry, as does *MFS* which also has a raised amplitude at ∼0°E (Fig. 3.2g). Note also that the eddy identified in *GLO* in Fig. 2.1 occupies this same position, and a large eddy here is visible in the corresponding gridded altimetry map (not shown).
10 Cyclone and anticyclone radii are generally larger in the southern parts of the study domain than they are in the north (Fig. 3.2i-p). The patterns between the models and altimetry are very similar for the anticyclones, aside from the Balearic Sea in *ALT* where the radii are slightly larger. There is more variability in the cyclones, where *GLO* has noticeably smaller radii in the Alboran gyres. *ALT* and *IBI* cyclone radii are
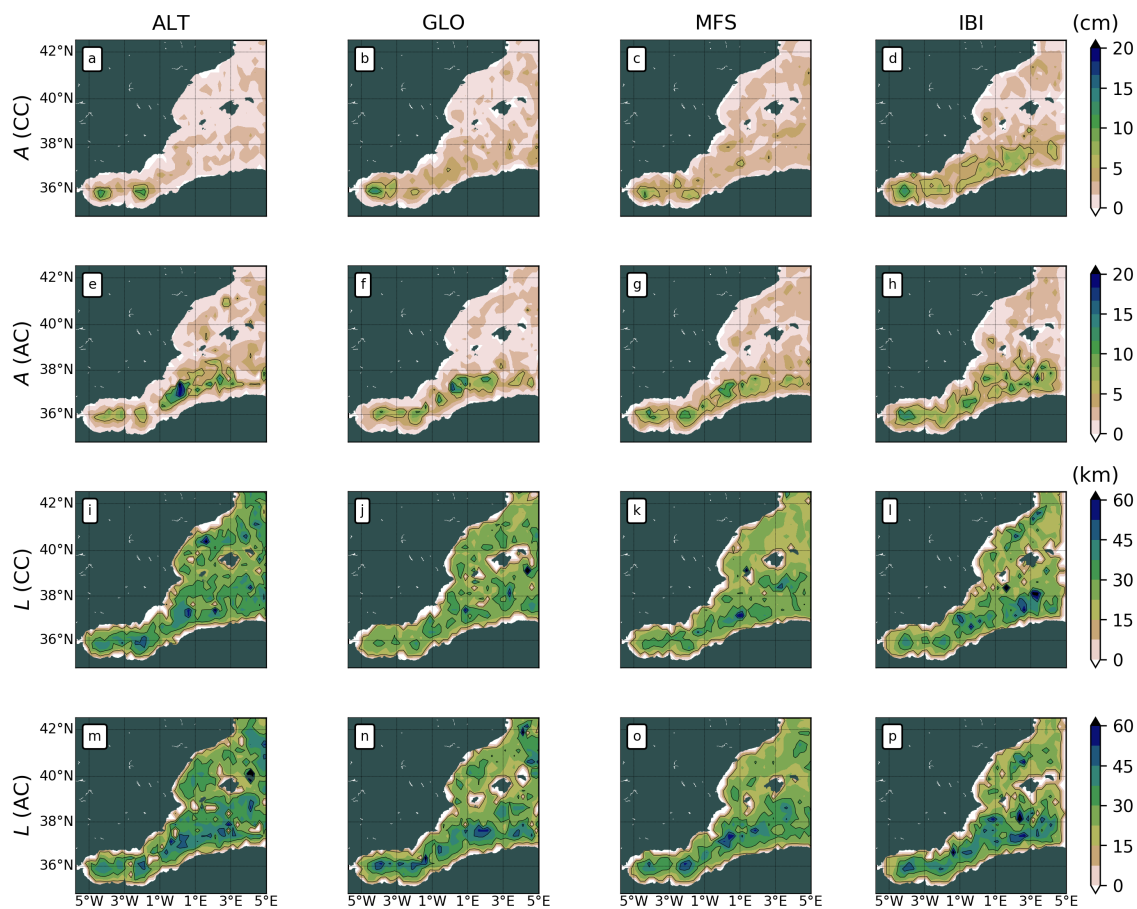
Figure 4. Maps of mean eddy amplitude (a-h) and radius (i-p) over the western Mediterranean. Columns for *ALT*, *GLO*, *MFS* and *IBI*. Top and bottom paired rows for cyclones (CC) and anticyclones (AC).

marginally larger than their counterparts in *GLO* and *MFS*. Differences in radii for eddies of both signs between *ALT* and the models are most apparent in the Balearic Sea, where *ALT* eddies are consistently larger.

Eddy intensity maps from all products show progressive increases with resolution in both cyclones and
5   anticyclones (Fig. 3.3a-h). *EI* is consistently at or above 0.2 cm km^{-1} within the Alboran Sea. In *ALT* the western and eastern Alboran gyres are clearly distinguishable in the *EI* signal. *ALT* cyclones along the Algerian coast to the east have weak *EI*, whereas anticyclones have some of the largest values. Examination of Fig. 3.2a,e indicates this variability is largely determined by eddy amplitude rather than radius.

3.2   Subregional eddy composites

10   In this section we focus on the anticyclones in the western and eastern Alboran gyres (WAG and EAG) and the Cartagena frontal region (CRT) to the east. As anticyclones are the dominant signal in the Alboran Sea we omit cyclones from our analysis. (We do however provide the cyclonic counterparts to the vertical section figures in this section in Supp. **??**) Horizontal and vertical eddy composites illustrate the variability in vorticity, temperature and salinity across the Alboran Sea subregions. This sea is the most energetic region
15   of the western Mediterranean. The topography in the Alboran Sea is steep to the north, west and south (see inset in Fig. 1.1) with maximum gradients of above 25° (e.g., Costello et al., 2010). A shallow undersea ridge known as the Alboran Ridge extends northeastward from Cape Three Forks towards the center of the EAG; the 0.7 km^2 Alboran Island is found on the ridge at -3.0°W, 35.9°N. The Alboran Trough is a deep water channel along the northern base of the ridge that connects the western and eastern basins. Mass exchange
20   with the north Atlantic takes place at the open Strait of Gibraltar to the west, and to the east with the wider western Mediterranean. A summary of the eddy properties from the eddy tracker for these subregions is provided in Tab. 2

3.2.1   Horizontal subregional eddy composites

Horizontal anticyclonic eddy composites of ς/f, T' and S' in Fig. 3.4 reveal the intensity of the eddy
25   property anomalies of the three defined subregions of the Alboran Sea. Each anomaly is plotted at the median positions of the eddy coordinates that contribute to each subregion. The median eddy positions between the models are very similar. In the WAG the eddy positions are in the deepest waters in the center of the gyre;
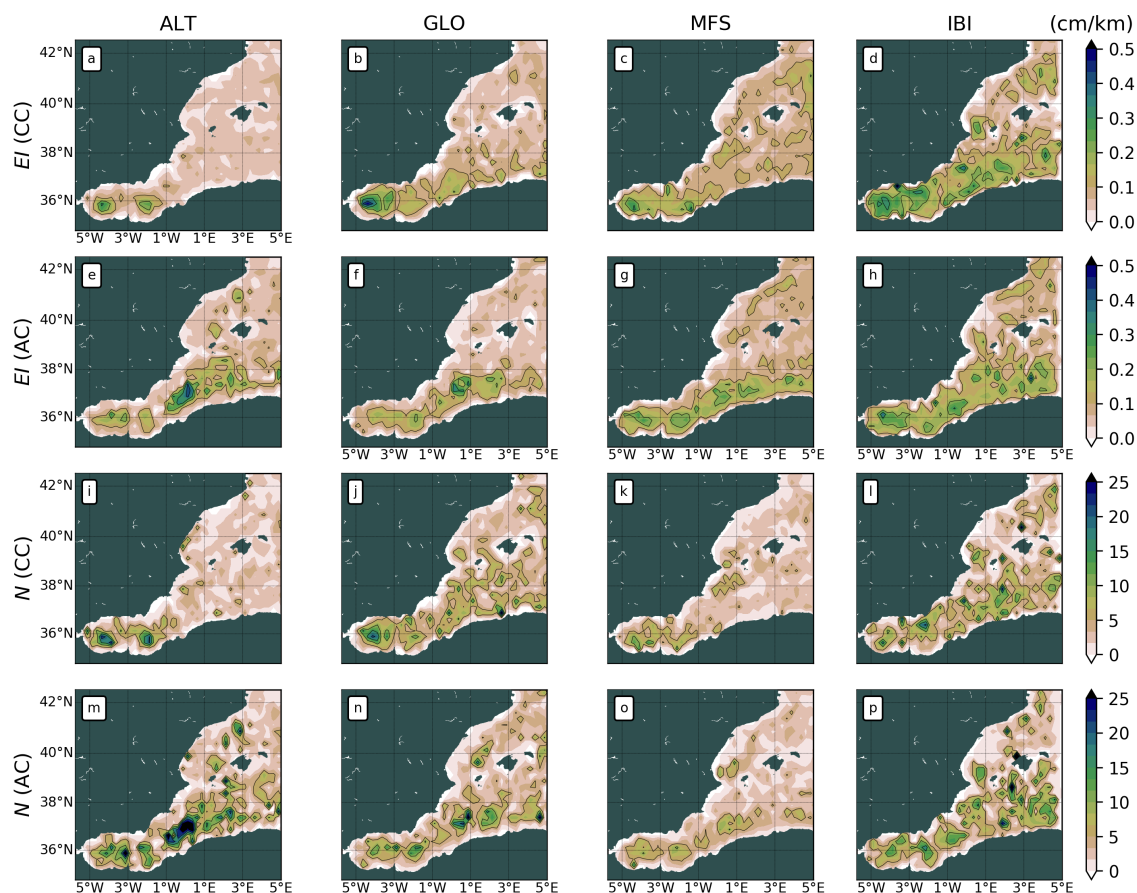
Figure 5. Maps of mean eddy intensity (a-h) and nonlinearity (i-p) over the western Mediterranean. Columns for *ALT*, *GLO*, *MFS* and *IBI*. Paired rows for cyclones (CC) and anticyclones (AC). Maps of the numerator (U) and denominator (c) for nonlinearity in i through p are shown in Supp. **??**.

Table 2. Subregional mean and median coordinates and properties from the eddy tracker for anticyclones in the western Alboran gyre (WAG), eastern Alboran gyre (EAG), and the Cartagena frontal region (CRT). $\bar{\cdot}$ and $\widetilde{\cdot}$ denote the respective means and medians of eddy positional coordinates (degrees) and radii (km) in each subregion defined in Fig. 1.1.

Subregion	Model	$\overline{Lon}$	$\overline{Lat}$	$\widetilde{Lon}$	$\widetilde{Lat}$	$\bar{L}$	$\widetilde{L}$
WAG	GLO	-4.11	36.02	-4.06	36.03	33.2	29.2
	MFS	-4.12	35.90	-4.18	35.85	30.6	29.5
	IBI	-4.24	35.84	-4.26	35.74	28.9	25.3
EAG	GLO	-2.34	35.90	-2.27	35.86	34.5	32.0
	MFS	-2.23	35.92	-2.17	35.91	33.3	31.1
	IBI	-2.36	35.92	-2.26	35.91	33.9	31.8
CRT	GLO	-0.50	36.66	-0.43	36.64	31.6	28.9
	MFS	-0.67	36.64	-0.71	36.67	35.4	26.0
	IBI	-0.66	36.68	-0.68	36.65	35.4	32.8

GLO is found north of the Vizconde de Eza seamount (located at $\sim$4°W, 35.8°N in Fig. 1.1), while *MFS* and *IBI* are to its west. In the EAG the eddy positions, lying over the southern 1000 m isobath of the eastern Alboran basin, are virtually indistinguishable. The CRT coordinates are located about 0.75° further north in the broad deep water depression that opens into the Algerin basin with, again, little observable difference in

5 median eddy position between the models. The plotting depth in Fig. 3.4 of each anomaly corresponds to the respective absolute maximum in the water column at the eddy centre. These depths are variable, being very shallow for ζ, some tens of meters deeper for T', and generally below 100 m for S'. The anomalies tend to be approximately confined within the limits of the two radius estimates, L and L_e. The anomalies are plotted out to a radial extent of $2L$, with the region between L and $2L$ defined as the *eddy impact region*

10 (e.g., Frenger et al., 2015).

The near surface negative vorticity anomalies inside the L/L_e radius are variable according to both subregion and model in Fig. 3.4 (top row). Between subregions intensity successively decreases from the WAG to CRT, while for the models there is an increase from *GLO* to *IBI*. The model increase can be explained

by the increasing model resolution. In the WAG, *IBI* $|\zeta/f|$ approaches 1 indicating the possible admittance of ageostrophic motions; however, the incoming Atlantic Jet in *IBI* is suspected to be too strong such that these ζ values may be an overestimate. Outside of the eddy radius (i.e., from approximately L to $2L$) the ζ anomalies are uniformly positive.

5   The temperature anomalies in the middle row of Fig. 3.4 vary in depth between $\sim$20 and 155 m. There is inconsistency between the models in terms of the depths in each subregion. For example, the shallowest anomaly in *MFS* is in the WAG, whereas *IBI* has its *deepest* anomaly in this subregion. The most intense values of T' are found in *GLO* in the WAG. In the eddy impact region of this eddy composite there is intense negative T' in the southern and western quadrants; on the eastern side there is an abrupt transition to an arc of positive T' over the Alboran Trough at $\sim$3.5°W. The *MFS* WAG pattern is similar although the strength of the anomaly is smaller. *IBI* has a strong T' core, with a nearly continuous negative T' in the eddy impact region. The EAG and CTR T' patterns are quite consistent between the models, although the *IBI* CRT T' is noticeably stronger than in the other models.

The salinity anomalies in the bottom row of Fig. 3.4 are the most consistent of the three variables. The
15   deepest anomalies are in the WAG, and the shallowest in the CRT. The fresh S' composites in the eddy cores have similar magnitudes, and the same for the opposite sign in the eddy impact region. In contrast to temperature, the same sign S' in the impact region is found both south and north of the eddy cores. The most intense S' is in the WAG in *IBI* at a depth of 155 m; this contrasts with *GLO* and *MFS* minima at 130 and 123 m, respectively.

20 ### 3.2.2   Vertical subregional eddy composites

3.2.3   Western Alboran Gyre

Vertical sections through zonal and meridional anticyclonic WAG eddy composites in Fig. 3.5 reveal good structural agreement between the models in ζ/f, T' and S'. There are also some striking differences. The widths of the anomalies broadly correspond to the mean radii marked in orange in Fig. 3.5 for each eddy
25   composite (Tab. 2). The *tilt* of the eddies is described by the vertical brown lines; tilt is estimated based on the position of absolute maximum ζ within the eddy radius at each vertical level. (See Sec. 2.5 and Supp. **??**.)
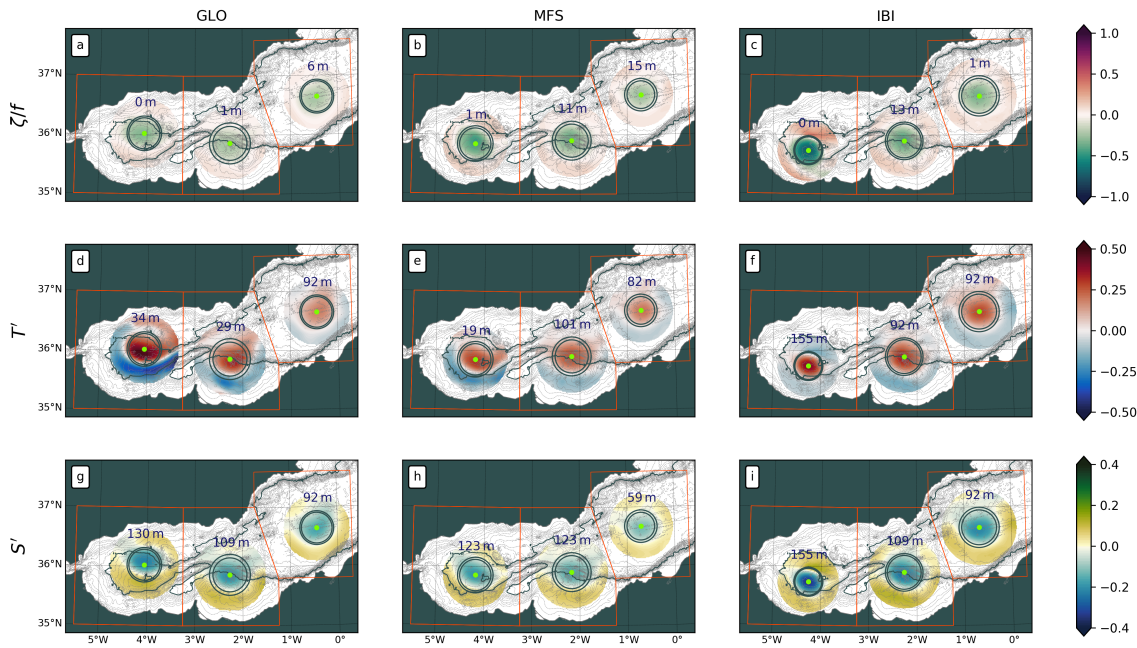
Figure 6. Anticyclonic eddy composites of ς/f (top row), T' (middle row), and S' (bottom row) in three subregions in the Alboran Sea from the three CMEMS models, *GLO* (left column), *MFS* (middle column) and *IBI* (right column). Orange boxes indicate the bounds of each subregion used for the compositing. The median position of each eddy composite is shown by neon green dots; the depth in meters at which each composite is plotted corresponds to absolute maximum of the variable over the water column at the position of the eddy center. Gray circles around each dot correspond to the median speed and effective eddy radii. SRTM topographic contours are plotted in gray from the surface to the bottom at intervals of 100 m; the 1000 m isobath is plotted in dark gray.

There is good agreement in eddy tilt between the models, especially in the meridional composites. The median radii are around 9% smaller than the means in Tab. 2.

Concerning the eddy composite topography, the zonal plots indicate shoaling towards the Strait of Gibraltar in the west. The meridional plots show the eddies to be centered over the 200 m deep trough just to the north of the Alboran Ridge (see inset in Fig. 1.1) at the bottom of the Alboran basin. Owing to the successively higher model grid resolutions, more topographic details are visible in *IBI* and *MFS* than in *GLO*. The median *IBI* WAG position is to the west and south of the *MFS* and *GLO* positions; this explains the apparent shallower IBI topographic composite.

The intensity of surface-intensified negative ς/f more than doubles between *GLO* and *IBI*, and the anomalies extend downward to between $\sim$150 m (*GLO*) and $\sim$200 m (*IBI*) (top row Fig. 3.5).

GLO and *MFS* T' sections are quite similar with two positive cores, one between the surface and about 50 m, and the other at 110 m (middle row Fig. 3.5). The *IBI* section is distinct as it has just one core at 150 m, and no expression at the surface. The zonal sections have weak negative T' anomalies on their eastern flanks in the eddy impact area[1] beyond the radius. The strongest T' anomalies are seen in *GLO* (upper core) and *IBI*.

WAG S' from the models have similar structure in Fig. 3.5 (bottom row). Single cores of negative S' are centered at around 135 m. The upper surfaces of these anomalies shoal towards the north and east, producing a small surface expression within the northeast quadrant of each eddy.

3.2.4 Eastern Alboran Gyre

Structural agreement similar to that of the western Alboran gyre above is also visible in the vertical sections of ς/f, T' and S' in the eastern Alboran gyre (Fig. 3.6). The eddies here have marginally larger radii than in the WAG (Tab. 2), and lie in slightly deeper waters. The intensity of ς/f progressively increases from *GLO* to *IBI*. Zonal sections of ς/f are symmetric with weak tilt (top row Fig. 3.6); the eddies are centered over topography that descends towards the east. The meridional sections of ς/f are asymmetric with strong agreement between each model. The eddies tilt towards the north over the first $\sim$100-175 m, then back towards the south down to $\sim$600-700 m where they begin to feel the topography on their southern flanks.

---

[1]The eddy impact area is defined by Frenger et al. (2013) as the area between one and three times the eddy radius around the eddy center; here, given the size of the Alboran gyres and the confined Alboran domain, we choose to use twice the radius.
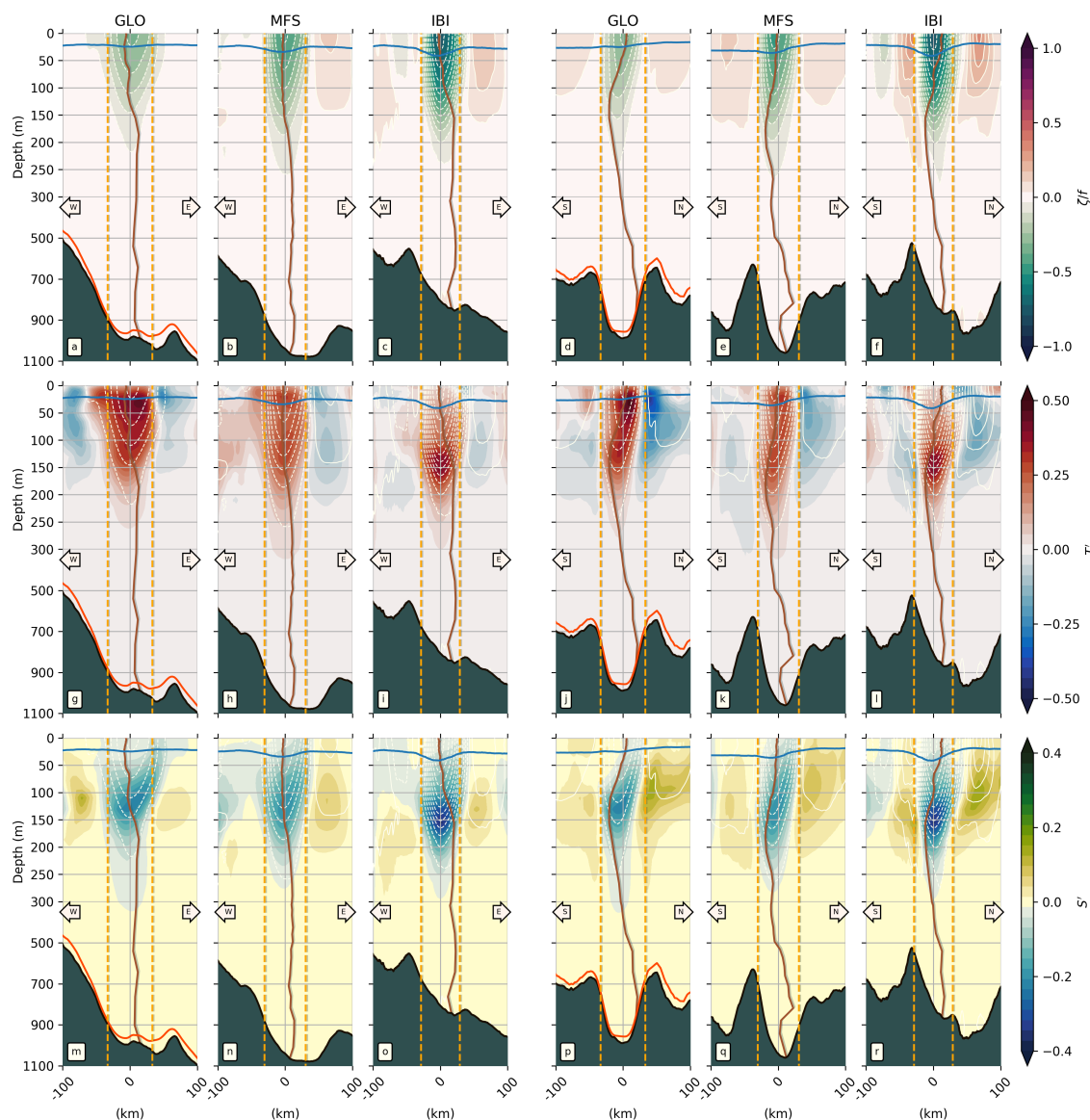
Figure 7. Eddy composite sections from *GLO*, *MFS* and *IBI* in the western Alboran gyre. Left-hand-side (right-hand-side) columns show zonal (meridional) sections of (top to bottom) relative vorticity, temperature anomalies and salinity anomalies, from the surface to the ocean floor. The central position of each section is the median of the longitudes and latitudes associated with the eddy observations used to make the composites (Tab. 2). Blue lines indicate the mixed layer depth; the dotted blue line corresponds to the MLD from the MFS model. The vertical brown line in each section is the vorticity-based tilt correction (see Sec. 2.5). Vertical orange dashed lines indicate the boundaries of each composite eddy based on its mean radius estimate from Tab. 2. Composite topographic profiles in black from SRTM, and in red from, respectively *GLO* and *IBI*. Note change of vertical scale at 300 m.

Table 3. Speed based radius statistics for eddies from the three models. Units km.

Product	Subregion	Rmin	Rmax	Rmean	Rmedian	Rmad
GLO	WAG	13.05	73.2	33.18	29.15	8.40
	EAG	13.10	108.75	34.92	32.28	10.38
	CRT	13.15	100.05	33.08	29.60	7.70
MFS	WAG	111	222	333	444	
	EAG	13.10	108.75	34.92	32.28	10.38
	CRT	111	222	333	444	555
IBI	WAG	999	28.93	25.25		
	EAG	13.10	108.75	34.92	32.28	10.38
	CRT	111	222	333	444	555

Both anomalies T' and S' in the EAG are slightly weaker than those of the WAG. In contrast to the WAG, zonal T' in *GLO* and *IBI* has a surface signature comparable to that below; *MFS* on the other hand has a weak surface signature that only becomes significant at about 30 m. The zonal S' structure is the reverse of T', in *GLO* and *IBI* the anomaly is centered between ∼50 and 150 m, then back towards the south down

5 to ∼600-700 m where they begin to feel the topography on their southern flanks. Both anomalies T' and S' in the EAG are slightly weaker than those of the WAG. In contrast to the WAG, zonal T' in *GLO* and *IBI* has a surface signature comparable to that below; *MFS* on the other hand has a weak surface signature that only becomes significant at about 30 m. The zonal S' structure is the reverse of T', in *GLO* and *IBI* the anomaly is centered between ∼ 50 and 150 m whereas in *MFS* it reaches the surface. The meridional

10 S' sections emphasize the strong northward tilt of the eddies. Negative S' is concentrated north of the eddy center between the surface and ∼100 m in each of the models.

EAG
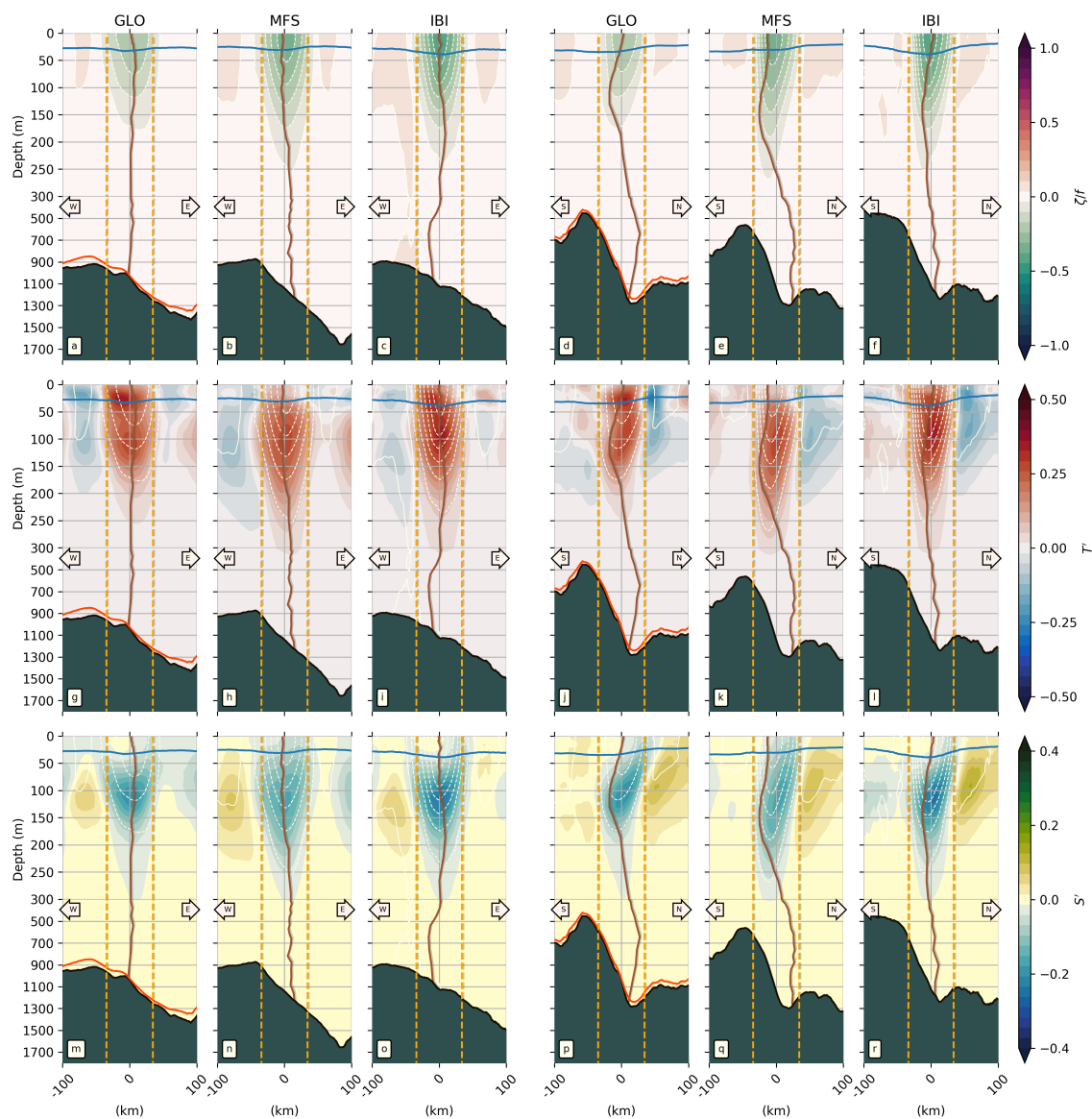
Figure 8. Same as Fig. 3.5 but for the eastern Alboran gyre.

3.2.5 Cartagena Frontal Region

Detected eddies in the Cartagena Frontal region to the east of the EAG have weaker tracer and circulation anomalies than in the Alboran gyres (Fig. 3.7). Eddy radii here from *GLO* and *MFS* are slightly smaller than in the WAG and EAG; the *IBI* CRT eddies meanwhile have the largest radii for all three subregions

5   (Tab. 2). Depths in the CRT reach 2500 m and seafloor gradients are smaller than those in the Alboran gyres of Figs. 3.5 and 3.6. The same ς/f intensity increase from *GLO* to *IBI* observed in the WAG and EAG is visible in Fig. 3.7 (top row). *MFS* and *IBI* ς/f zonal sections are symmetric with small tilt; *GLO* has pronounced westward tilt down to about 150 m The meridional ς/f sections are again asymmetric, with agreement between the models. The eddies tilt northward between the surface and ∼125 m. The eddies are

10   centered over the deepest isobath in both the zonal and meridional directions. Tracer anomalies T' and S' in the CRT are weaker than in the Alboran gyres. The cores with maximum T' are found at around 100 m depth in the three models, with *GLO* slightly deeper (Fig. 3.7j) and *MFS* shallower (Fig. 3.7k). In the upper ∼30 m T' is near zero in *GLO* and *MFS*, while *IBI* has a weak positive T' between the surface and ∼20 m. The vertical extents of the T' anomalies progress from around 250 m (*GLO*) to 800 m (*IBI*). The T' anomalies

15   are compensated by negative S' of broadly similar structure (Fig. 3.7m-r).

3.2.6 Seasonal mixed layer depth

Good agreement in the seasonal cycle of the WAG mixed layer depth between the models is evident in Fig. 3.8. The most interesting observation from the model estimates is the large variability, both seasonal as well as intra-seasonal, with the latter prominent in winter and autumn. As shortwave solar radiation

20   increases from spring to summer (Ruiz et al., 2008), it induces strong stratification that is maximum at the end of the summer, leading to shallow MLDs of between ∼5 and 15 m. In autumn, with decreasing shortwave radiation forcing, the MLD deepens to maxima of around 50 m (75 m for *IBI*). In winter, under the influence of wind-forced mixing processes, the model MLD estimates in the WAG are the deepest over the seasonal cycle, with *IBI* again having the maximum values with depths below 100 m. This large variability in

25   MLD over the course of a year may have important implications for upper layer processes, such as vertical motions associated with mesoscale structures (i.e., the WAG, and EAG) that promote exchange of mass,
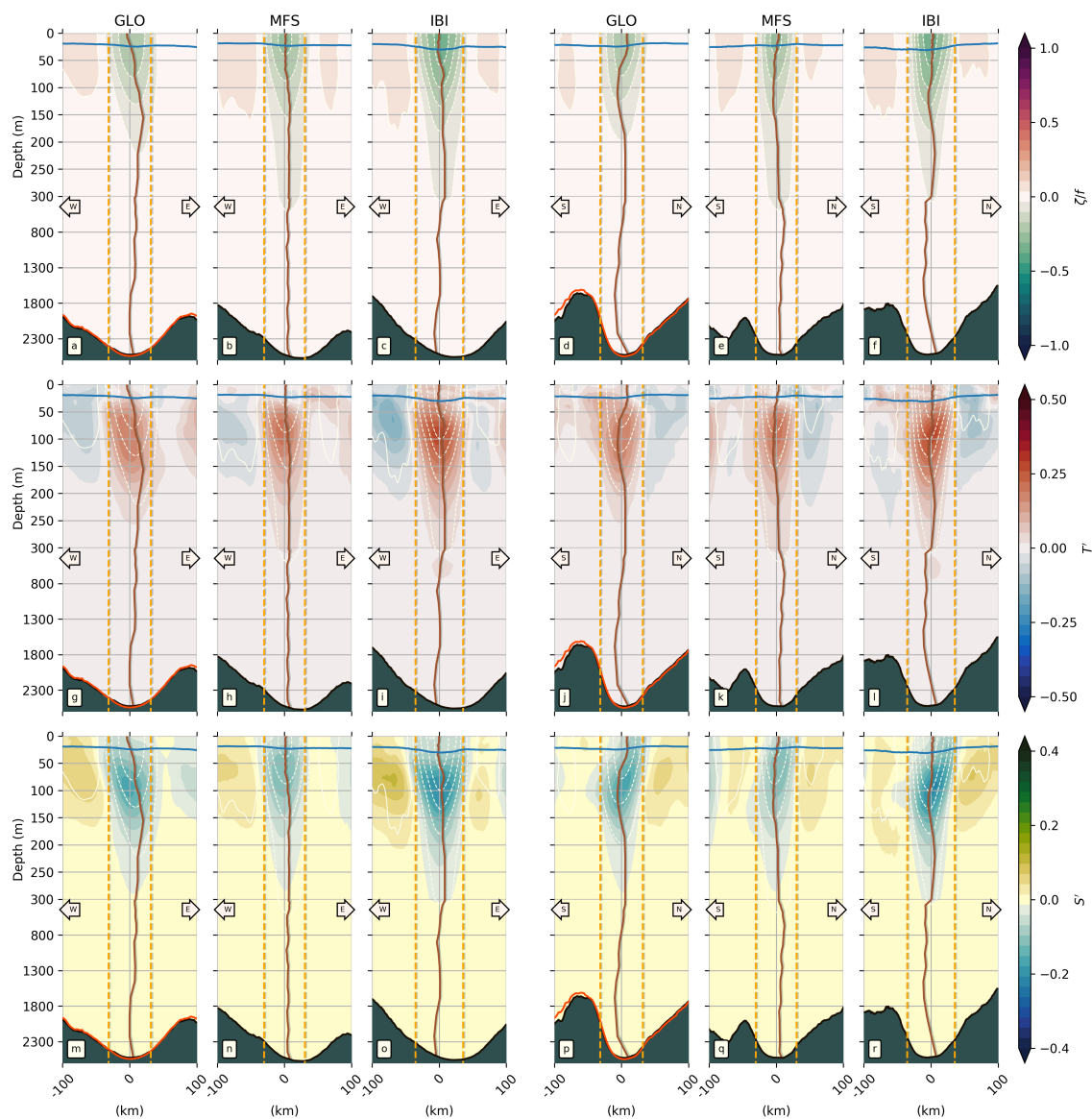
Figure 9. Same as Fig. 3.5 but for the Cartagena frontal region.

heat and tracers between the surface and the ocean interior. Seasonal MLD variability for the EAG and CRT subregions is similar to that shown for the WAG in Fig. 3.8; see Figs. **??** and S**??** in Supp. **??**.

4   Discussion and conclusions

To our knowledge this is the first time that an eddy tracker and eddy compositing techniques has been used

5   for an oceanic model intercomparison. Our results suggest that this approach can yield useful information concerning both the technical aspects of the models and characterisation of physical oceanographic features and structure.

   With respect to the technical aspects, we find that the main added value of the eddy composites is the insight that they provide into the choices made for the model configurations. *GLO* and *MFS* have data

10   assimilation, while *IBI* does not. *IBI* on the other hand has tides, but these are not included in *GLO* and *MFS*. While tides are generally not considered to be important in the Mediterranean Sea as a whole, they are relevant in the Alboran Sea and, furthermore, there have been many arguments for inclusion of tides in Mediterranean Sea model simulations (e.g., Harzallah et al., 2014; Naranjo et al., 2014). In the WAG in Fig. 3.5 we showed that *IBI* has a very small positive T' in the upper 75 m in comparison with *GLO* and

15   *MFS* which both have stronger positive T'. The most likely hypothesis for this discrepancy in the respective values of T' is the inclusion or not of tides. Hence *GLO* and *MFS* lack the tidal-induced vertical mixing across the WAG that is present in *IBI*, and that acts to cool the surface mixed layer. If this suggestion can be confirmed by the respective MFC engineers then a strong recommendation to include tides in future versions of *GLO* and *MFS* is warranted. Another secondary factor that could also contribute to the T' discrepancy is

20   the different bulk heat flux parameterisations used at the surface. These could also be revised by the MFC engineers.

   Model resolution clearly has an impact on the strength of the eddy properties and their ratios in Sec. 3.1, and the T, S and ζ composite anomalies in Sec. 3.2. The differences become apparent by comparison with the figures in Supp. **??** where the tilt correction is applied during the making of the composites. Notice the

25   larger numbers of ζ contours (white) in Figs. **??-??**, and also the negative ζ that extends all the way to the seabed in each of the models. Choice of model resolution depends obviously on the size of the domain to be used; for the moment it is unlikely that in the near future we will see the global *GLO* at the resolution of
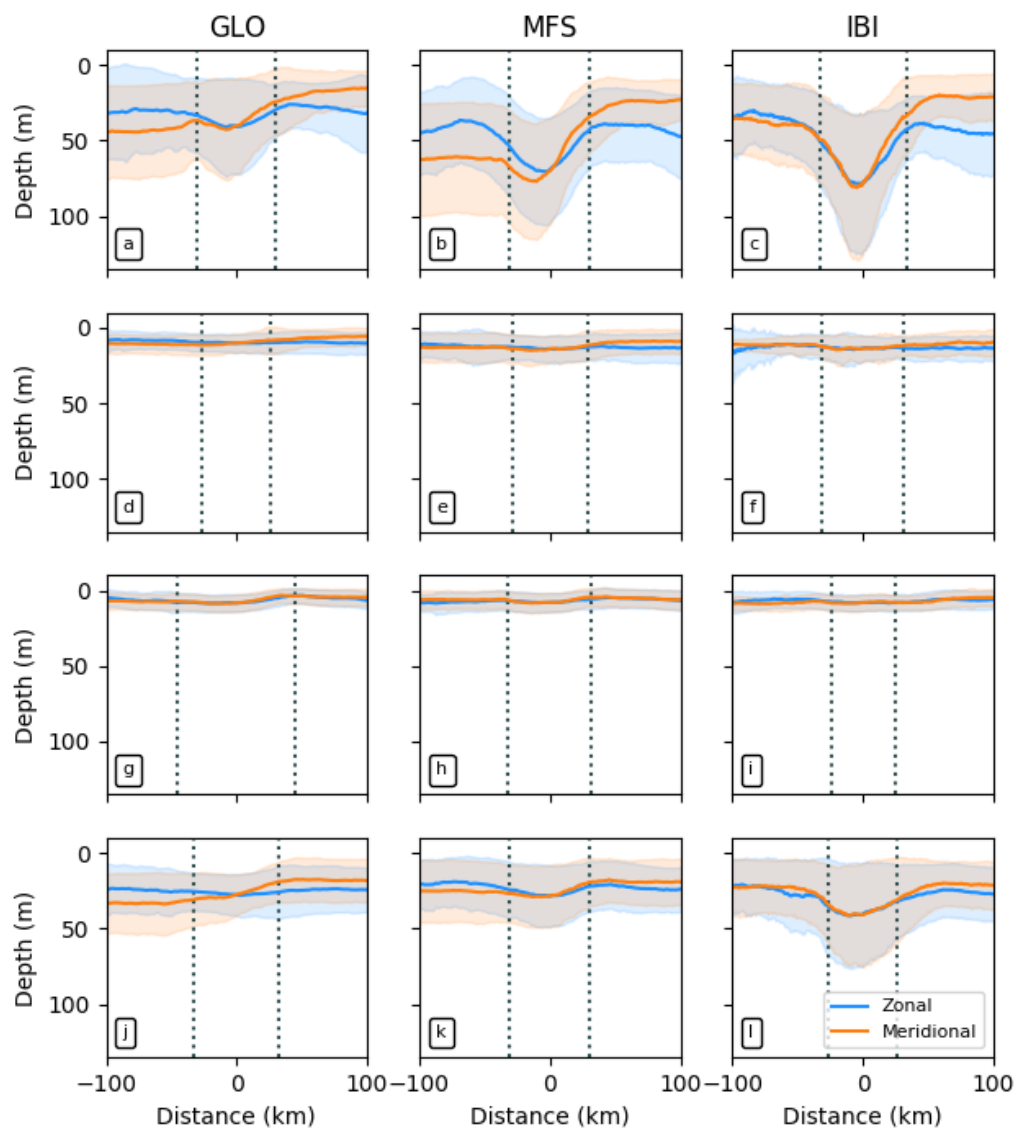
Figure 10. Mean and standard deviation of the seasonal mixed layer depth in anticyclones in the western Alboran gyre for *GLO* (left column), *MFS* (middle column) and *IBI* (right column). Zonal (meridional) profiles in blue (orange). Vertical dotted lines mark the mean eddy radius from the center.

IBI. On the other hand, the new version of *MFS* that was released during the writing of this paper in 2018 has a horizontal resolution of 0.042° (a 33% increase over the version used here) and double the number of vertical levels.

An important final point concerns validation. Our present operational *in situ* observing system in the

5 WMED is not yet able to provide sufficient density and frequency of observations for the creation of a reference eddy composite dataset. This is especially the case in the Alboran Sea where instrument residence times - Argo floats for instance - are very short owing to the large density gradients and associated strong currents. The current best approach is to use the CMEMS ARMOR3D product (as done by Mason et al., 2017, in the Brazil-Malvinas Confluence), but ARMOR3D is not presently recommended for the Mediterranean Sea. We

10 therefore cannot state at this moment how closely any of the eddy composite results in Figs. 3.4 through 3.7 may or may not correspond to reality.

New insight is provided into the mesoscale content of three CMEMS operational model products (*GLO*, *MFS* and *IBI*) using a robust, sea-surface-height-based eddy identification and tracking tool. The analysis period is 2013 through 2016. Maps for each model product of mean eddy properties, including position,

15 lifetime, radius and amplitude, reveal general consistency over the western Mediterranean Sea study region. The models that include data assimilation, *GLO* and *MFS*, approximate most closely the eddy property distributions observed with contemporaneous SSH observations from altimetry. Knowledge of eddy location enables construction of subregional 3D eddy composites of the model prognostic variables such as temperature, salinity and relative vorticity. Composites of these variables in three subregions of the Alboran Sea

20 reveal the strong frontal characteristics associated with the Alboran gyres. They also provide feedback about the impacts of inclusion of data assimilation, tides or other parameterisations in the respective model configurations. The eddy tracking tool and compositing analysis approach presented in this study is of benefit to CMEMS operational services because it enriches the CMEMS product menu with additional properties associated with the 2D circulation. Future versions of the CMEMS catalogue should also include other key

25 variables such as vertical velocity derived from models and/or observational products (e.g., ARMOR3D) at weekly or daily frequencies. Improvements in the CMEMS operational models will contribute to advances in characterisation and understanding of mesoscale physical processes and their role in the functioning of marine ecosystems.

Acknowledgments

This work was carried out as part of the Copernicus Marine Environment Monitoring Service (CMEMS) *MedSub* project. CMEMS is implemented by Mercator Ocean in the framework of a delegation agreement with the European Union. The Ssalto/Duacs altimeter products are produced and distributed by the Copernicus Marine and Environment Monitoring Service (CMEMS) (http://www.marine.copernicus.eu).

References

Copernicus Marine Environment Monitoring Service (CMEMS) Service Evolution Strategy: R&D priorities, Tech. rep., CMEMS Scientific and Technical Advisory Committee (STAC), http://marine.copernicus.eu/wp-content/uploads/2017/06/CMEMS-Service_evolution_strategy_RD_priorities_V3-final.pdf, 2017.

5 Allen, J. T., Smeed, D., Tintoré, J., and Ruiz, S.: Mesoscale subduction at the Almeria-Oran front: Part 1: Ageostrophic flow, J. Mar. Syst., 30, 263–285, https://doi.org/10.1016/S0924-7963(01)00062-8, 2001.

Amante, C. and Eakins, B. W.: ETOPO1 Global Relief Model converted to PanMap layer format, Tech. rep., NOAA-Natl. Geophys. Data Center PANGAEA, https://doi.org/10.1594/PANGAEA.769615, 2009.

Aulicino, G., Cotroneo, Y., Ruiz, S., Sánchez-Román, A., Pascual, A., Fusco, G., Tintoré, J., and Budillon, G.:
10 Monitoring the Algerian Basin through glider observations, satellite altimetry and numerical simulations along a SARAL/AltiKa track, Journal of Marine Systems, 179, 55–71, https://doi.org/10.1016/j.jmarsys.2017.11.006, 2018.

Aznar, R., Sotillo, M. G., Cailleau, S., Lorente, P., Levier, B., Amo-Baladrón, A., Reffray, G., and Alvarez Fanjul, E.: Strengths and weaknesses of the CMEMS forecasted and reanalyzed solutions for the Iberia-Biscay-Ireland (IBI) waters, J. Mar. Syst., 159, 1–14, https://doi.org/10.1016/j.jmarsys.2016.02.007, 2016.

15 Barnier, B., Madec, G., Penduff, T., Molines, J.-M., Treguier, A. M., Le Sommer, J., Beckmann, A., Biastoch, A., Böning, C., Dengg, J., Derval, C., Durand, E., Gulev, S., Remy, E., Talandier, C., Theetten, S., Maltrud, M. E., McClean, J. L., and De Cuevas, B.: Impact of partial steps and momentum advection schemes in a global ocean circulation model at eddy-permitting resolution, Ocean Dynam., 56, 543–567, https://doi.org/10.1007/s10236-006-0082-1, 2006.

Becker, J. J., Sandwell, D. T., Smith, W. H. F., Braud, J., Binder, B., Depner, J., Factor, J., Ingalls, S., Kim, S.-H.,
20 Ladner, R., Marks, K., Nelson, S., Pharaoh, A., Trimmer, J., Von Rosenberg, J., Wallace, G., and Weatherall, P.: Global Bathymetry and Elevation Data at 30 Arc Seconds Resolution: SRTM30_PLUS, Journal of Marine Geodesy, 32, 355–371, https://doi.org/10.1080/01490410903297766, 2009.

Bergamasco, A. and Malanotte-Rizzoli, P.: The circulation of the Mediterranean Sea: a historical review of experimental investigations, Adv. Oceanogr. Limnol., 1, 11–28, https://doi.org/10.1080/19475721.2010.491656, 2011.

25 Bethoux, J. P. and Gentili, B.: Functioning of the Mediterranean Sea: past and present changes related to freshwater input and climate changes, Journal of Marine Systems, 20, 33–47, https://doi.org/10.1016/S0924-7963(98)00069-4, 1999.

Bosse, A., Testor, P., Mortier, L., Prieur, L., Taillandier, V., DÓrtenzio, F., and Coppola, L.: Spreading of Levantine Intermediate Waters by submesoscale coherent vortices in the northwestern Mediterranean Sea as observed with
30 gliders, J. Geophys. Res. Oceans, 120, 1599–1622, https://doi.org/10.1002/2014JC010263, 2015.

Chelton, D. B., Gaube, P., Schlax, M. G., Early, J. A., and Samelson, R. M.: The Influence of Nonlinear Mesoscale Eddies on Near-Surface Oceanic Chlorophyll, Science, 334, 328–332, https://doi.org/10.1126/science.1208897, 2011.

Costello, M. J., Cheung, A., and De Hauwere, N.: Surface Area and the Seabed Area, Volume, Depth, Slope, and Topographic Variation for the World's Seas, Oceans, and Countries, Environ. Sci. Technol., 44, 8821–8828, https://doi.org/10.1021/es1012752, 2010.

Cotroneo, Y., Aulicino, G., Ruiz, S., Pascual, A., Budillon, G., Fusco, G., and Tintoré, J.: Glider and satellite high resolution monitoring of a mesoscale eddy in the Algerian basin: Effects on the mixed layer depth and biochemistry, Journal of Marine Systems, 162, 73–88, https://doi.org/10.1016/j.jmarsys.2015.12.004, 2016.

Dai, A., Qian, T., Trenberth, K. E., and Milliman, J. D.: Changes in Continental Freshwater Discharge from 1948 to 2004, Journal of Climate, 22, 2773–2792, https://doi.org/10.1175/2008JCLI2592.1, 2009.

de Boyer Montégut, C., Madec, G., Fischer, A. S., Lazar, A., and Iudicone, D.: Mixed layer depth over the global ocean: An examination of profile data and a profile-based climatology, J. Geophys. Res. Oceans, 109, C12003, https://doi.org/10.1029/2004JC002378, 2004.

Dobricic, S. and Pinardi, N.: An oceanographic three-dimensional variational data assimilation scheme, Ocean Modelling, 22, 89–105, https://doi.org/10.1016/j.ocemod.2008.01.004, 2008.

Dombrowsky, E., Bertino, L., Brassington, G. B., Chassignet, E. P., Davidson, F., Hurlburt, H. E., Kamachi, M., Lee, T., Martin, M. J., Mei, S., and Tonani, M.: GODAE Systems in Operation, Oceanography, 22, 80–95, https://doi.org/10.2307/24860992, http://www.jstor.org/stable/24860992, 2009.

D'Ortenzio, F., Iudicone, D., de Boyer Montégut, C., Testor, P., Antoine, D., Marullo, S., Santoleri, R., and Madec, G.: Seasonal variability of the mixed layer depth in the Mediterranean Sea as derived from in situ profiles, Geophys. Res. Lett., 32, L12605, https://doi.org/10.1029/2005GL022463, 2005.

Egbert, G. and Erofeeva, S. Y.: Efficient Inverse Modeling of Barotropic Ocean Tides, J. Atmos. Oceanic Technol., 19, 183–204, https://doi.org/10.1175/1520-0426(2002)019<0183:EIMOBO>2.0.CO;2, 2002.

Fekete, B. M., Vorosmarty, C. J., and Grabs, W.: Global, Composite Runoff Fields Based on Observed River Discharge and Simulated Water Balances, Tech. Rep. 22, Global Runoff Data Center (World Meteorological Organization), Koblenz, Germany, 1999.

Frenger, I., Gruber, N., Knutti, R., and Münnich, M.: Imprint of Southern Ocean eddies on winds, clouds and rainfall, Nat. Geosci., 6, 608–612, https://doi.org/10.1038/ngeo1863, 2013.

Frenger, I., Münnich, M., Gruber, N., and Knutti, R.: Southern Ocean eddy phenomenology, J. Geophys. Res. Oceans, 120, 7413–7449, https://doi.org/10.1002/2015JC011047, 2015.

Harzallah, A., Alioua, M., and Li, L.: Mass exchange at the Strait of Gibraltar in response to tidal and lower frequency forcing as simulated by a Mediterranean Sea model, Tellus A: Dynamic Meteorology and Oceanography, 66, 1–21, https://doi.org/10.3402/tellusa.v66.23871, 2014.

Hernandez, F., Blockley, F., Brassington, G. B., Davidson, F., Divakaran, P., Drévillon, M., Ishizaki, S., Garcia-Sotillo, M., Hogan, P. J., Lagemaa, P., Levier, B., Martin, M., Mehra, A., Mooers, C., Ferry, N., Ryan, A., Regnier, C., Sellar, A., Smith, G. C., Sofianos, S., Spindler, T., Volpe, G., Wilkin, J., Zaron, E. D., and Zhang, A.: Recent progress in performance evaluations and near real-time assessment of operational ocean products, Journal of Operational Oceanography, 8, s221–s238, https://doi.org/10.1080/1755876X.2015.1050282, 2015.

Herrmann, M. J., Bouffard, J., and Béranger, K.: Monitoring open-ocean deep convection from space, Geophysical Research Letters, 36, https://doi.org/10.1029/2008GL036422, 2009.

Holte, J. and Talley, L.: A New Algorithm for Finding Mixed Layer Depths with Applications to Argo Data and Subantarctic Mode Water Formation, J. Atmos. Oceanic Technol., 26, 1920–1939, https://doi.org/10.1175/2009JTECHO543.1, 2009.

Kurian, J., Colas, F., Capet, X. J., McWilliams, J. C., and Chelton, D. B.: Eddy properties in the California Current System, J. Geophys. Res. Oceans, 116, C08027, https://doi.org/10.1029/2010JC006895, 2011.

Le Traon, P.-Y., Dibarboure, G., Jacobs, M., Martin, M., Remy, E., and Schiller, A.: Use of Satellite Altimetry for Operational Oceanography, chap. 18, p. 28, Taylor & Francis Group, 2017.

Leaman, K. D. and Schott, F. A.: Hydrographic Structure of the Convection Regime in the Gulf of Lions: Winter 1987, Journal of Physical Oceanography, 21, 575–598, https://doi.org/10.1175/1520-0485(1991)021<0575:HSOTCR>2.0.CO;2, 1991.

Locarnini, R. A., Mishonov, A. V., Antonov, J. I., P., B. T., Garcia, H. E., Baranova, O. K., Zweng, M. M., Paver, C., Reagan, J. R., Johnson, D. R., Hamilton, M., and Seidov, D.: World Ocean Atlas 2013, Volume 1: Temperature, techreport 73, S. Levitus, Ed., A. Mishonov Technical Ed., NOAA Atlas NESDIS, https://doi.org/10.7289/V5F769GT, http://www.nodc.noaa.gov/OC5/indprod.html, 2013.

Lyard, F., Lefevre, F., Letellier, T., and Francis, O.: Modelling the global ocean tides: modern insights from FES2004, Ocean Dynam., 56, 1616–7341, https://doi.org/10.1007/s10236-006-0086-x, 2006.

Madec, G.: NEMO Ocean Engine (Note du Pole de Modélisation), Tech. Rep. 27, Institut Pierre-Simon Laplace (IPSL), iSSN 1288-1619, 2008.

Mason, E. and Pascual, A.: Multiscale variability in the Balearic Sea: an altimetric perspective, J. Geophys. Res. Oceans, 118, 3007–3025, https://doi.org/10.1002/jgrc.20234, 2013.

Mason, E., Pascual, A., and McWilliams, J. C.: A New Sea Surface Height Based Code for Oceanic Mesoscale Eddy Tracking, J. Atmos. Oceanic Technol., 31, 1181–1188, https://doi.org/10.1175/JTECH-D-14-00019.1, 2014.

Mason, E., Pascual, A., Gaube, P., Ruiz, S., Pelegrí, J. L., and Delepoulle, A.: Subregional characterization of mesoscale eddies across the Brazil-Malvinas Confluence, Journal of Geophysical Research - Oceans, 122, 3329–3357, https://doi.org/10.1002/2016JC012611, 2017.

Naranjo, C., García-Lafuente, J., Sannino, C., and Sánchez-Garrido, J. C.: How much do tides affect the circulation of the Mediterranean Sea? From local processes in the Strait of Gibraltar to basin-scale effects, Progress in Oceanography, 127, 108–116, https://doi.org/10.1016/j.pocean.2014.06.005, 2014.

Pascual, A., Ruiz, S., Olita, A., Troupin, C., Claret, M., Casas, B., Mourre, B., Poulain, P.-M., Tovar-Sanchez, A., Capet, A., Mason, E., Allen, J. T., Mahadevan, A., and Tintoré, J.: A Multiplatform Experiment to Un-ravel Meso- and Submesoscale Processes in an Intense Front (AlborEx), Frontiers in Marine Science, 4, 39, https://doi.org/10.3389/fmars.2017.00039, 2017.

Puillat, I., Taupier-Letage, I., and Millot, C.: Algerian Eddies lifetime can near 3 years, J. Mar. Syst., 31, 245–259, https://doi.org/10.1016/S0924-7963(01)00056-2, 2002.

Pujol, M.-I. ., Faugère, Y., Taburet, G., Dupuy, S., Pelloquin, C., Ablain, M., and Picot, N.: DUACS DT2014: the new multi-mission altimeter data set reprocessed over 20 years, Ocean Sci., 12, 1067–1090, https://doi.org/dx.doi.org/10.5194/os-12-1067-2016, 2016.

Renault, L., Oguz, T., Pascual, A., Vizoso, G., and Tintoré, J.: Surface circulation in the Alborán Sea (western Mediterranean) inferred from remotely sensed data, J. Geophys. Res. Oceans, 117, C08009, https://doi.org/10.1029/2011JC007659, 2012.

Rio, M.-H., Pascual, A., Poulain, P.-M., Menna, M., Barceló-Llull, B., and Tintoré, J.: Computation of a new mean dynamic topography for the Mediterranean Sea from model outputs, altimeter measurements and oceanographic in situ data, Ocean Science, 10, 731–744, https://doi.org/10.5194/os-10-731-2014, 2014.

Robinson, A. R. and Golnaraghi, M.: The Physical and Dynamical Oceanography of the Mediterranean Sea, vol. 419, Springer, https://doi.org/10.1007/978-94-011-0870-6_12, 1994.

Ruiz, J., Echevarría, F., Font, J., Ruiz, S., Garcia, E., Blanco, M. J., Jiménez-Goméz, F., Prieto, L., Gonzáles-Alaminos, A., Garcia, C. M., Cipollini, P., Snaith, H., Bartual, A., Reul, A., and Rodríguez, V.: Surface distribution of chloro-phyll, particles and gelbstoff in the Atlantic jet of the Alborán Sea: from submesoscale to subinertial scales of vari-ability, Journal of Marine Systems, 29, 277–292, https://doi.org/10.1016/S0924-7963(01)00020-3, 2001.

Ruiz, S., Gomis, D., Sotillo, M. G., and Josey, S. A.: Characterization of surface heat fluxes in the Mediter-ranean Sea from a 44-year high-resolution atmospheric data set, Global Planet. Change, 63, 258–274, https://doi.org/10.1016/j.gloplacha.2007.12.002, 2008.

Smith, W. H. F. and Sandwell, D. T.: Global sea floor topography from satellite altimetry and ship depth soundings, Science, 277, 1956–1962, https://doi.org/10.1126/science.277.5334.1956, 1997.

Sotillo, M. G., Cailleau, S., Lorente, P., Levier, B., Reffray, G., Amo-Baladrón, A., Benkiran, M., and Alvarez Fanjul, E.: The MyOcean IBI Ocean Forecast and Reanalysis Systems: operational products and roadmap to the future Copernicus Service, Journal of Operational Oceanography, 8, 63–79, https://doi.org/10.1080/1755876X.2015.1014663, 2015.

Tintoré, J., La Violette, P. E., Blade, I., and Cruzado, A.: A Study of an Intense Density Front in the Eastern Alboran Sea: The Almeria–Oran Front, J. Phys. Oceanogr., 18, 1384–1397, https://doi.org/10.1175/1520-0485(1988)018<1384:ASOAID>2.0.CO;2, 1988.

Tonani, M., Balmaseda, M., Bertino, L., Blockley, E., Brassington, G. B., Davidson, F., Drillet, Y., Hogan, P. J., Kuragano, T., Lee, T., Mehra, A., Paranathara, F., Tanajura, C. A. S., and Wang, H.: Status and future of global and regional ocean prediction systems, Journal of Operational Oceanography, 8, 201–220, https://doi.org/10.1080/1755876X.2015.1049892, 2015.

Vargas-Yáñez, M., Plaza, F., Garcia-Lafuente, J. M., Sarhan, T., Vargas, J. M., and Vélez-Belchí, P.: About the seasonal variability of the Alboran Sea circulation, Journal of Marine Systems, 35, 229–248, https://doi.org/10.1016/S0924-7963(02)00128-8, 2002.

Von Schukmann, K., Le Traon, P.-Y., Alvarez Fanjul, E., Axell, L., Balmaseda, M., Breivik, L.-A., Brewin, J. W., Bricaud, C., Drevillon, M., Drillet, Y., Dubois, C., Embury, O., Etienne, H., García Sotillo, M., Garric, G., Gasparin, F., Gutknecht, E., Guinehut, S., Hernandez, F., Juza, M., Karlson, B., Korres, G., Legeais, J.-F., Levier, B., Lien, V., Morrow, R., Notarstefano, G., Parent, L., Pascual, A., Pérez-Gómez, B., Perruche, C., Pinardi, N., Pisano, A., Poulain, P.-M., Pujol, I. M., Raj, R. P., Raudsepp, U., Hervé Roquet, H., Samuelsen, A., Sathyendranath, S., She, J., Simoncelli, S., Solidoro, C., Tinker, J., Tintoré, J., Viktorsson, L., Ablain, M., Almroth-Rosell, E., Bonaduce, A., Clementi, E., Cossarini, G., Dagneaux, Q., Desportes, C., Dye, S., Fratianni, C., Good, S., Greiner, E., Gourrion, J., Hamon, M., Holt, J., Hyder, P., Kennedy, J., Manzano-Muñoz, F., Melet, A., Meyssignac, B., Mulet, S., Buongiorno Nardelli, B., O'Dea, E., Olason, E., Paulmier, A., Pérez-González, I., Reid, R., Racault, M.-F., Raitsos, D. E., Ramos, A., Sykes, P., Szekely, T., and Nathalie Verbrugge, N.: The Copernicus Marine Environment Monitoring Service Ocean State Report, Journal of Operational Oceanography, 9, s235–s320, https://doi.org/10.1080/1755876X.2016.1273446, 2016.

Zweng, M. M., Reagan, J. R., Antonov, J. I., Locarnini, R. A., Mishonov, A. V., Boyer, T. P., Garcia, H. E., Baranova, O. K., Johnson, D. R., Seidov, D., and Biddle, M. M.: World Ocean Atlas 2013, Volume 2: Salinity, techreport 74, S. Levitus, Ed.; A. Mishonov, Technical Ed.; NOAA Atlas NESDIS, http://www.nodc.noaa.gov/OC5/indprod.html, 2013.